Assessing the Influence of Convective Downdrafts and Surface Enthalpy Fluxes on Tropical Cyclone Intensity Change in Moderate Vertical Wind Shear

LEON T. NGUYEN[a]

National Research Council, and NOAA/Atlantic Oceanographic and Meteorological Laboratory/Hurricane Research Division, Miami, Florida

ROBERT ROGERS

NOAA/Atlantic Oceanographic and Meteorological Laboratory/Hurricane Research Division, Miami, Florida

JONATHAN ZAWISLAK AND JUN A. ZHANG

NOAA/Atlantic Oceanographic and Meteorological Laboratory/Hurricane Research Division, and Rosenstiel School of Marine and Atmospheric Science, University of Miami, Miami, Florida

(Manuscript received 30 December 2018, in final form 27 June 2019)

ABSTRACT

The thermodynamic impacts of downdraft-induced cooling/drying and downstream recovery via surface enthalpy fluxes within tropical cyclones (TCs) were investigated using dropsonde observations collected from 1996 to 2017. This study focused on relatively weak TCs (tropical depression, tropical storm, category 1 hurricane) that were subjected to moderate (4.5–11.0 m s^{-1}) levels of environmental vertical wind shear. The dropsonde data were analyzed in a shear-relative framework and binned according to TC intensity change in the 24 h following the dropsonde observation time, allowing for comparison between storms that underwent different intensity changes. Moisture and temperature asymmetries in the lower troposphere yielded a relative maximum in lower-tropospheric conditional instability in the downshear quadrants and a relative minimum in instability in the upshear quadrants, regardless of intensity change. However, the instability increased as the intensification rate increased, particularly in the downshear quadrants. This was due to increased boundary layer moist entropy relative to the temperature profile above the boundary layer. Additionally, significantly larger surface enthalpy fluxes were observed as the intensification rate increased, particularly in the upshear quadrants. These results suggest that in intensifying storms, enhanced surface enthalpy fluxes in the upshear quadrants allow downdraft-modified boundary layer air to recover moisture and heat more effectively as it is advected cyclonically around the storm. By the time the air reaches the downshear quadrants, the lower-tropospheric conditional instability is enhanced, which is speculated to be more favorable for updraft growth and deep convection.

1. Introduction

Despite marginal, but statistically significant improvements in tropical cyclone (TC) intensity forecasts over recent decades (DeMaria et al. 2014), TC intensity forecasting remains a significant challenge. One important influence on TC intensity change is the vertical shear of the environmental flow. Climatological studies have shown that as the magnitude of the environmental vertical wind shear increases, TC intensification becomes less likely (e.g., DeMaria and Kaplan 1994; Kaplan and DeMaria 2003; Kaplan et al. 2010; 2015). Given its important influence on TC intensity change, the interaction of TCs with vertical wind shear has long been an area of intense research interest.

Several recent studies have shown that TC intensity change in the presence of environmental vertical wind shear can be quite unpredictable, particularly within moderate shear that is neither too strong to completely prevent intensification nor too weak to exert a negligible impact on intensity change. Using an ensemble of high-resolution simulations, Tao and Zhang (2015) examined how the predictability of TC intensity changed within

[a] Current affiliation: Oregon State University, Corvallis, Oregon.

Corresponding author: Leon T. Nguyen, lnguyen0427@gmail.com

DOI: 10.1175/MWR-D-18-0461.1

different magnitudes of shear. When no shear was imposed, all of the simulations underwent rapid intensification (RI) at approximately the same time. When 7.5 m s^{-1} of shear was imposed, all of the simulations failed to significantly intensify. However, when 5–6 m s^{-1} of shear was imposed, the simulated TC intensity exhibited much more variability, indicating decreased predictability in the moderate shear regime. Zhang and Tao (2013) also found decreased predictability when the shear magnitude was approximately 5 m s^{-1}. In a study of operational forecasts in the Atlantic basin, Bhatia and Nolan (2013) showed that the largest mean absolute error in the National Hurricane Center's (NHC) official intensity forecasts occurred with TCs that were experiencing 10–20 kt (5.1–10.3 m s^{-1}) of shear and had an initial intensity of at least 70 kt (36 m s^{-1}). In terms of forecast skill, they found that across all initial intensity bins, the official intensity forecasts were less skillful within the moderate shear range (10–20 kt) than within the high (>20 kt) and low (<10 kt) shear bins. This predictability challenge has been recognized even outside the meteorological community. In its report on the sinking of the *El Faro* cargo ship in moderately sheared Hurricane Joaquin (2015), the National Transportation Safety Board (NTSB) recommended that the National Oceanic and Atmospheric Administration (NOAA) "develop and implement a plan specifically designed to emphasize improved model performance in forecasting tropical cyclone track and intensity in moderate-shear environments" (Sumwalt et al. 2017). This provides ample motivation for improving our understanding of how individual TCs are affected differently by environmental vertical wind shear, particularly moderate shear.

Shear can have a deleterious impact on TCs through a number of possible mechanisms, including the tilting of the vortex away from vertical alignment and subsequent lack of realignment (Jones 1995), intrusion of low entropy air into the vortex in the midtroposphere (Simpson and Riehl 1958; Cram et al. 2007; Tang and Emanuel 2010), the intrusion of low entropy air into the boundary layer via downdrafts (Riemer et al. 2010, 2013; Tang and Emanuel 2010; Molinari et al. 2013; Riemer and Laliberté 2015), and the outward fluxes of potential vorticity and equivalent potential temperature in the upper troposphere (Frank and Ritchie 2001). Observational composite studies have also shown that the interaction of vertical wind shear with the TC vortex is often associated with decreased azimuthal symmetry in precipitation and deep convection, with the maximum in precipitation and deep convection generally occurring in the downshear-left quadrant and greatly reduced precipitation and deep convection generally occurring in the upshear quadrants (e.g., Corbosiero and Molinari 2002; Chen et al. 2006; Hence and Houze 2011; Hence and Houze 2012; Reasor et al. 2013; DeHart et al. 2014). This decrease in symmetry can limit the projection of the diabatic heating onto the symmetric component, which has been shown to be key for TC intensification by idealized (Nolan and Grasso 2003; Nolan et al. 2007) and observational composite studies (Rogers et al. 2013; Alvey et al. 2015; Tao et al. 2017; Shimada et al. 2017; Fischer et al. 2018).

There are a number of factors on various spatial scales that can modulate the TC intensity response to environmental vertical wind shear. On the vortex scale, the ability of the vortex to become better vertically aligned after being tilted away from the upright position is an important factor. The reduction of vortex tilt in some sheared TCs has been attributed to several hypothesized mechanisms, including vortex precession into the upshear quadrants (Jones 1995), vortex Rossby wave damping (Schecter et al. 2002; Reasor et al. 2004; Reasor and Montgomery 2015), and downshear reformation or vortex merger processes (Molinari et al. 2004; Molinari and Vollaro 2010; Nguyen and Molinari 2015; Chen et al. 2018; Rios-Berrios et al. 2018). On the large scale, the shape of the vertical profile of the environmental flow can be another influence. In their idealized simulations, Finocchio et al. (2016) found that TCs were more likely to intensify both when the vertical shear was distributed over a deeper layer of the troposphere and when the vertical shear was higher in the troposphere. Onderlinde and Nolan (2016) found in their simulations that TCs were more likely to intensify when the environmental flow exhibited positive TC-relative helicity. Climatological studies, however, do not show a clear relationship between shear height/depth or TC-relative helicity and subsequent TC intensification (Finocchio and Majumdar 2017; Rios-Berrios and Torn 2017).

In addition to kinematic influences, there are also a number of thermodynamic factors that can determine whether a sheared storm will intensify or not. In their observational study of Hurricane Edouard (2014), Zawislak et al. (2016) found that as Edouard intensified, the midtroposphere became progressively more humid in the upshear quadrants. A climatological study of storms in moderate shear by Rios-Berrios and Torn (2017) showed that intensifying storms had more midtropospheric moisture than steady-state storms, particularly on the upshear side. Humidification of the upshear quadrants can limit dry air entrainment into developing updrafts, allowing them to grow and persist as they propagate azimuthally around the TC center. The recovery of downdraft-modified boundary layer air through surface enthalpy fluxes from the ocean can also help a TC become resistant to shear. Observations analyzed by Zhang et al. (2013) and Molinari et al. (2013) supported the following sequence of events: Convective downdrafts associated with asymmetrically distributed convection act to cool and dry

TABLE 1. Number of dropsondes in the full dropsonde dataset listed by year, agency/field campaign, aircraft, and basin. This study includes dropsondes deployed during National Oceanic and Atmospheric Administration (NOAA), National Aeronautics and Space Administration (NASA), and Office of Naval Research (ONR) field campaigns.

Years	Agency/field campaign program	Aircraft	Basin	Sondes
1996–2017	NOAA	G-IV	NATL/EPAC	9099
1996–2017	NOAA	P-3	NATL/EPAC	7172
2008	ONR TCS-08	C-130/P-3/Falcon	WPAC	1436
2012–14	NASA HS-3	Global Hawk	NATL	1251
2015	ONR TCI	WB-57	NATL/EPAC	786
2010	ONR ITOP	C-130/DOTSTAR	WPAC	771
2015–16	NOAA SHOUT	Global Hawk	NATL/EPAC	722
2010	NASA GRIP	DC-8	NATL	296
2006	NASA NAMMA	DC-8	NATL	178
2017	NOAA/NASA EPOCH	Global Hawk	NATL/EPAC	125
2001	NASA CAMEX-4	DC-8, ER-2	NATL	107

the lower troposphere in the left of shear quadrants. As the boundary layer air is advected azimuthally around the storm, it extracts moisture and heat through surface latent and sensible heat fluxes from the ocean, until moist entropy reaches a maximum downshear right, where convection typically initiates in a sheared storm. Idealized modeling studies by Rappin and Nolan (2012) and Onderlinde and Nolan (2016) found that the surface fluxes in the upshear and left of shear regions were larger in the intensifying storms than the nonintensifying storms. They hypothesized that these enhanced surface fluxes helped the downdraft-cooled boundary layer recover faster, contributing to the growth and persistence of convection into the upshear quadrants of the intensifying storms. The importance of surface fluxes is further supported by the Rios-Berrios and Torn (2017) climatological study, which also showed stronger surface latent heat fluxes in the intensifying cases compared to the steady-state cases. Additional recent studies of moderately sheared Hurricane Edouard (2014) found that a reduction in surface enthalpy fluxes occurred due to sea surface cooling in the downshear-right quadrant, contributing to a decrease in deep convection and the subsequent weakening of the storm's intensity (Rogers et al. 2016; Zhang et al. 2017). In summary, the vertical alignment of the vortex, the thermodynamic state of the midtroposphere and the boundary layer, as well as the moistening of the latter through surface enthalpy fluxes from the ocean can all help determine whether a moderately sheared storm will intensify or not.

The main scientific goal of this study is to evaluate the effects of cooling/drying by convective downdrafts and the subsequent downstream recovery via surface enthalpy fluxes on the intensity change of moderately sheared storms, particularly storms of weaker intensities (tropical depression, tropical storm, or category 1 hurricane intensity). Because Bhatia and Nolan (2013) showed that the statistical and dynamical model intensity forecast skill improved with increasing initial intensity, the current study focuses on storms of weaker intensities that are less predictable. Moderately sheared storms of weaker intensities have been investigated in a number of recent observational case studies (e.g; Rogers et al. 2016; Zawislak et al. 2016; Nguyen et al. 2017; Zhang et al. 2017), but in this study, we examine these storms within a composite framework using dropsonde observations. Prior observational composite studies (Reasor et al. 2013; Zhang et al. 2013) have focused primarily on intense ($>49\,m\,s^{-1}$) storms, rather than the weaker storms assessed in this study.

The paper will be organized as follows. Section 2 describes the data and methods used in this study. Section 3 gives an overview of the lower-tropospheric moisture and temperature distribution relative to the shear vector within different intensity change regimes. Sections 4 and 5 detail the lower-tropospheric convective instability and surface enthalpy flux differences between intensity change regimes, respectively. Section 6 summarizes the results and places them in the context of recent published work.

2. Data and methods

This study predominantly uses data from GPS dropsondes, which are instruments that provide vertical profiles of atmospheric pressure, temperature, humidity, wind speed, and wind direction as they descend from the aircraft down to the sea surface (Hock and Franklin 1999). Dropsondes released in tropical cyclones worldwide during the years 1996–2017 were used. Table 1 shows the dropsonde distribution among various field campaigns that comprise the database used in this study. All NOAA, National Aeronautics and Space Administration (NASA), and Office of Naval Research (ONR) field campaign sondes used in this study were processed using the National Center for Atmospheric Research's (NCAR) Atmospheric Sounding Processing Environment (ASPEN) software. The NOAA sonde data from 1996 to 2009 were extracted from the NOAA Hurricane

Dropsonde Archive, organized by the NCAR/Earth Observing Laboratory (UCAR/NCAR–Earth Observing Laboratory 2017), and thus already underwent additional quality-control procedures described by Wang et al. (2015). The remaining NOAA sondes from 2010 to 2017 were postprocessed at NOAA Hurricane Research Division (HRD). All NASA and ONR sondes [with the exception of the NASA East Pacific Origins and Characteristics of Hurricanes (EPOCH) campaign] also underwent manual quality-control conducted by the Earth Observing Laboratory (EOL) at NCAR. After the above postprocessing procedures, all sondes used in this study were inspected visually for errors that were not yet identified. Any sondes that exhibited obviously unrealistic temperature, humidity, pressure, or wind speed profiles were removed from the study. Examples of unrealistic errors include near-surface temperature or dewpoint values that were at least 10 K higher or lower than immediately adjacent vertical levels, or near-surface wind speeds that were over 10 m s^{-1} larger than the observed TC intensity at that time. Sondes containing near-surface layers that were both saturated and nearly dry-adiabatic in terms of temperature lapse rate were corrected following the methodology of Bogner et al. (2000).

All of the dropsonde data listed in Table 1 comprise a developmental version of the Tropical Cyclone Dropsonde Research and Operations Product Suite (TC-DROPS), which was used in this study. TC-DROPS not only includes the postprocessed dropsonde data itself, but also includes information regarding the storm intensity and the storm's environment in order to facilitate tropical cyclone research and operational activities (Zawislak et al. 2018). The procedures described in the remainder of this section were applied during the development of the TC-DROPS dataset. Sonde locations were transformed into TC-relative coordinates using the flight-level circulation centers made available by HRD (at 2-min time resolution) computed using the methodology of Willoughby and Chelmow (1982). Each sonde's average TC-relative latitude–longitude position was used to classify sondes by quadrant within the storm. As sondes fall from the aircraft down to the sea surface, they are displaced horizontally by the horizontal wind, otherwise known as "sonde drift." This sonde drift can cause individual sondes to be erroneously identified as being in one particular quadrant of the storm, when in reality, the sonde may have drifted into the adjacent quadrant. The 50th and 95th percentiles of the distance between the sonde's average position and the sonde's splash position were 2.54 and 7.05 km, respectively. Given these relatively small displacements and the uncertainty of the shear direction itself (resulting from the choice of method and dataset in the shear calculation), sonde drift did not have a significant impact on the composite analyses presented in this manuscript. The sonde data were interpolated to 10-m vertical resolution below 2-km altitude, and to 50-m vertical resolution above 2-km altitude.

The 850–200 hPa environmental vertical wind shear magnitude and direction were extracted from the Statistical Hurricane Intensity Prediction Scheme (SHIPS) developmental database (DeMaria and Kaplan 1994; DeMaria et al. 2005). This shear was computed by averaging the 850 and 200 hPa winds within the 500 km radius using the wind fields from the Climate Forecast System Reanalysis (CFSR) (prior to 2000) or the Global Forecast System (GFS) operational analyses (from 2000 onward). It should be noted that using the shallower 850–500 hPa shear in this study yielded very similar results (not shown), with the exception of one notable difference that will be discussed later in the manuscript.

The sondes were classified by TC intensity and 850–200 hPa shear by referencing the nearest 6-hourly time in the NHC best track (Landsea and Franklin 2013) and SHIPS developmental databases, respectively. The sea surface temperature (SST) at each sonde's splash point was estimated using the nearest grid point of the Group for High Resolution Sea Surface Temperature (GHRSST) global Level 4 sea surface temperature analysis, produced daily at 0.25° resolution (Reynolds et al. 2007). This analysis incorporates data from the Advanced Very High Resolution Radiometer (AVHRR) as well as in situ ship and buoy observations. Although this SST dataset likely does not fully represent the upwelling of cooler water that occurs within the storm, this is mitigated somewhat because this study includes only storms that were of tropical depression, tropical storm, or category 1 hurricane intensity, whose winds are too weak to cause significant upwelling (Cione and Uhlhorn 2003).

This study included dropsondes that met all of the following criteria. First, the dropsonde had to be located within a TC that had an intensity less than or equal to 80 kt (41.2 m s^{-1}) (i.e., tropical depressions, tropical storms, and category 1 hurricanes). The TC also had to be experiencing 4.5–11.0 m s^{-1} of environmental vertical wind shear, defined as the 25th and 75th percentile of shear experienced by TCs globally (Rios-Berrios and Torn 2017). To remove cases occurring over relatively cold water, such as subtropical cyclones and TCs undergoing extratropical transition, only dropsondes collocated with an SST of at least 25°C were used. Dropsondes within TCs that made landfall within the subsequent 24-h time period were eliminated. Next, only dropsondes located within 25–200 km of the TC center were used. The inner 25 km were omitted in order to remove any eyelike soundings, and also to ensure that the sondes were accurately classified by shear-relative quadrant, given the uncertainty in

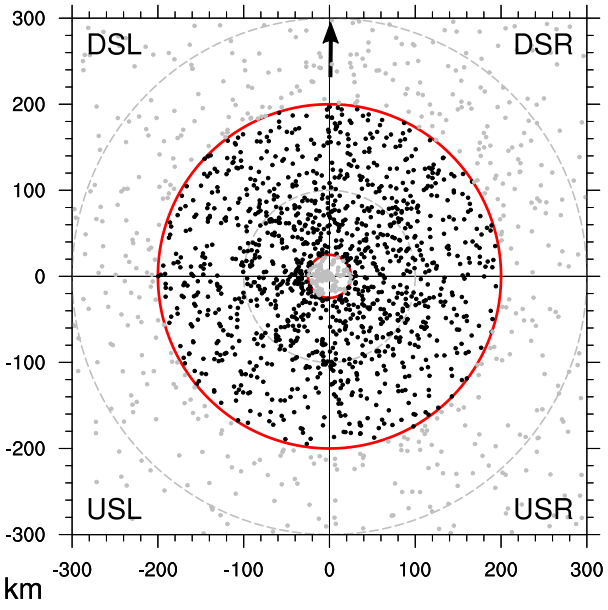

FIG. 1. Dropsonde positions in TCs that were ≤80 kt in intensity and experienced 4.5–11.0 m s^{-1} of shear at the time of the dropsonde observation. The inner and outer red circles denote the 25- and 200-km radii, respectively. Black dots show the profile-averaged TC-relative position of dropsondes located within the 25–200 km radii region. Shear vector is directed toward the top of the figure.

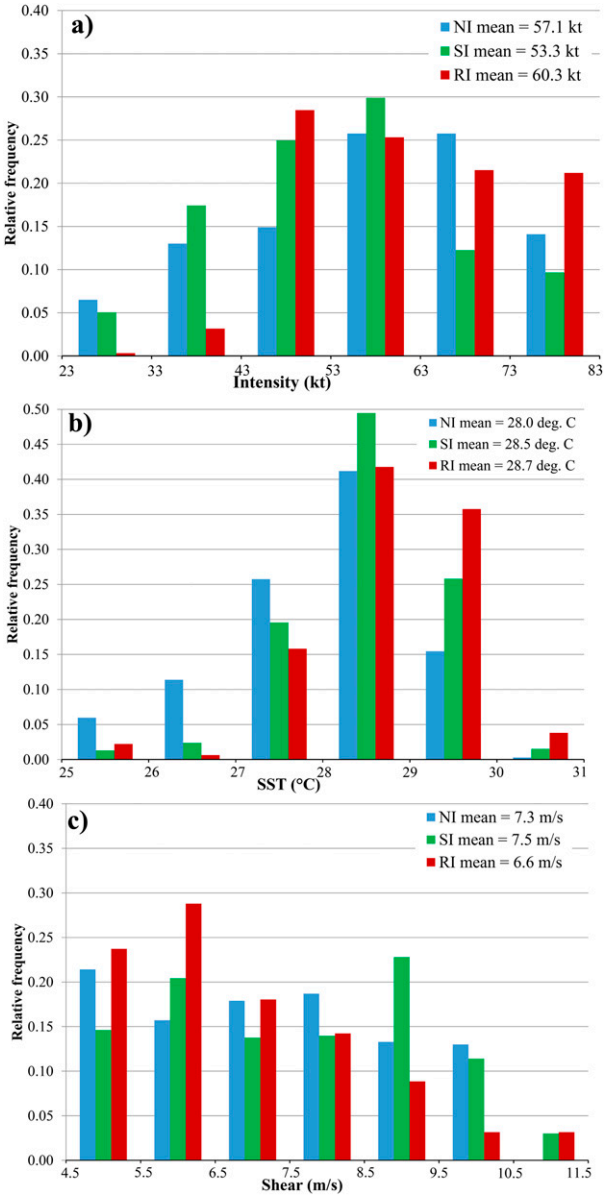

FIG. 2. Frequency distribution of dropsondes in each intensity change bin according to (a) TC intensity, (b) sea surface temperature, and (c) shear magnitude. Rapidly intensifying (RI) is defined as $\Delta V_{0\text{–}24h} \geq +20$ kt, slowly intensifying (SI) is defined as $+5 \leq \Delta V_{0\text{–}24h} \leq +15$ kt, and nonintensifying (NI) is defined as $\Delta V_{0\text{–}24h} \leq 0$ kt.

the flight-level TC center location. Because this study focuses on the processes occurring within the TC as a result of the shear, the outer radius of sondes used in this study was set subjectively at 200 km. Finally, dropsondes that exhibited a 0–1-km-averaged TC-relative wind speed of weaker than 10 m s^{-1} and were located within 75 km of the TC center were discarded from the study, as these sondes were likely more representative of the TC center. It should be noted that the dropsonde data in this study were not normalized with respect to the radius of maximum wind (RMW). Although a number of prior composite studies have normalized data with respect to the RMW within intense TCs in order to account for varying TC size, the RMW is often ill-defined and much less physically meaningful in weaker, more asymmetric TCs such as the ones assessed in this study (Nguyen et al. 2014; Leighton et al. 2018).

Figure 1 shows the profile-averaged TC-relative positions of the 1150 dropsondes that met the above criteria, rotated with respect to the shear vector. These dropsondes were further subdivided by 0–24 h TC intensity change, which is defined as the difference between the intensity at the nearest 6-hourly time in the NHC best track and the intensity 24 h after that time. As a result, the 0–24 h intensity change is given in 5 kt increments. The 0–24 h intensity change groups are defined as follows: Rapidly intensifying ($\Delta V_{0\text{–}24h} \geq +20$ kt), slowly intensifying ($+5 \leq \Delta V_{0\text{–}24h} \leq +15$ kt), and nonintensifying ($\Delta V_{0\text{–}24h} \leq 0$ kt). Note that the +20 kt (24 h)$^{-1}$ threshold differs from the traditional +30 kt (24 h)$^{-1}$ threshold for rapid intensification (Kaplan and DeMaria 2003; Kaplan et al. 2010) in order to make the sample sizes among the three subgroups as close to equal as possible. Also note that the nonintensifying cases include both steady-state and weakening cases.

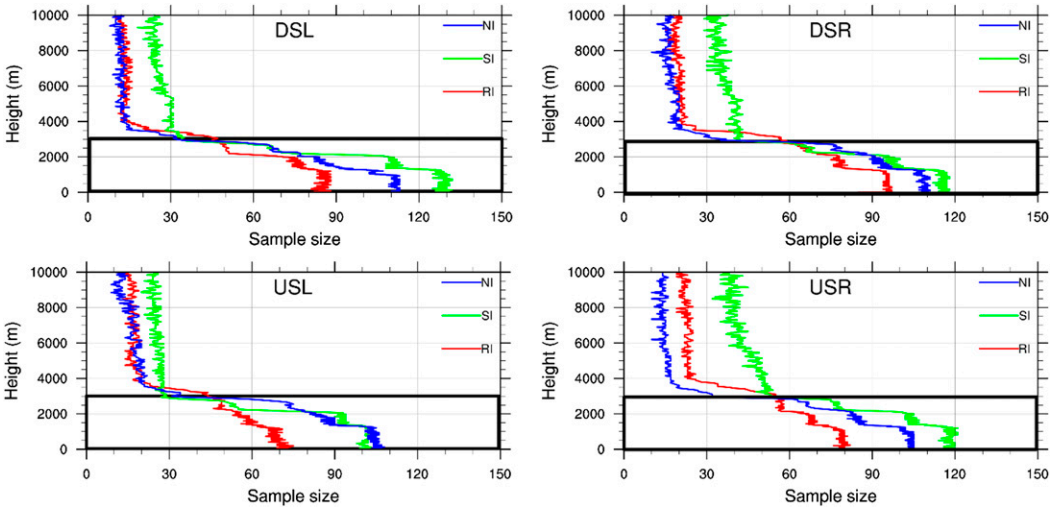

FIG. 3. Number of dropsonde observations at each altitude in each shear-relative quadrant for nonintensifying (NI, blue), slowly intensifying (SI, green), and rapidly intensifying (RI, red) cases. Shear vector is directed toward the top of the figure. This study focused on the lower troposphere, indicated by the black boxes.

Figure 2 shows the frequency distribution of sondes in each intensity change category according to TC intensity, SST, and shear magnitude. The rapid intensification (RI) sondes have a stronger mean intensity and an intensity distribution that is more skewed toward higher intensities than the slow intensification (SI) and nonintensification (NI) sondes. The RI sondes also have a mean SST that is 0.7°C warmer than the NI sondes, and there is a comparatively smaller (larger) proportion of RI sondes with a SST cooler than 27°C (warmer than 29°C), respectively. There were discernable differences in shear magnitude between the RI, SI, and NI cases, with the RI sondes having a smaller mean shear magnitude and a distribution slightly more skewed toward lower shear values. All of the aforementioned differences in the mean intensity, SST, and shear magnitude were statistically significant at the 95% confidence level as determined through a bootstrap method (e.g., Wilks 1995). The aim of this study is to explore whether the thermodynamic structure within the storm itself exhibits any substantial differences between intensity change groups.

Dropsondes that met the above criteria were then classified into shear-relative quadrants: downshear right (DSR), downshear left (DSL), upshear left (USL), and upshear right (USR). Figure 3 shows the dropsonde sample size with height in each shear-relative quadrant for each intensity change bin. Note that the sample size drops off precipitously above approximately 2-km altitude. This dropoff is because most of the sondes within the 25–200 km radii region were released from the P-3 aircraft, which typically flies between 2 and 4 km altitude. A much smaller proportion of sondes were released from high-altitude aircraft such as the G-IV, WB-57, DC-8, and Global Hawk (Table 1), illustrating the dearth of (and need for) observations in the middle and upper part of the troposphere within tropical cyclones. The current study utilizes observations predominantly in the lower troposphere (where the sample size is maximized) to assess the lower-tropospheric thermodynamic structure of moderately sheared storms in a shear-relative framework.

3. Lower-tropospheric moisture and temperature

Figure 4 shows the equivalent potential temperature (θ_e) and saturation equivalent potential temperature (θ_{es}) averaged in each shear-relative quadrant for the RI, SI, and NI storms. In the RI cases (Fig. 4a), the USR quadrant had the highest 0–1-km mean θ_e, while the USL quadrant had the lowest 0–1-km mean θ_e. The difference between these quadrants was about 2–3 K, and this difference was statistically significant at the 95% confidence level using a bootstrap method. Similarly, the mean θ_{es} also reached a maximum in the right of shear quadrants and a minimum in the left of shear quadrants, with a θ_{es} difference of about 2–4 K that was statistically significant at the 95% level. Above 1-km altitude, the θ_e differences between the quadrants (particularly DSR, DSL, USL) were less apparent. However, the θ_{es} quadrant differences were larger, with the mean θ_{es} in the USR quadrant significantly exceeding that of the DSL quadrant by 4–6 K at 2–3 km altitude. Because θ_e is a function of both moisture and temperature, the observed azimuthal variations of θ_e could be attributed to either moisture differences, temperature differences, or a combination of

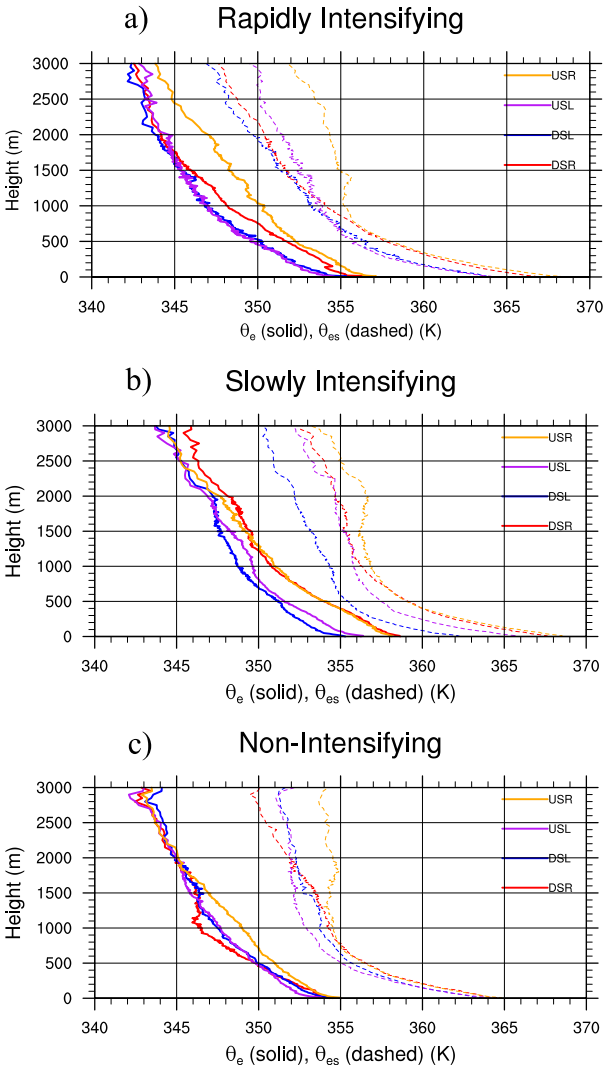

FIG. 4. Quadrant-mean equivalent potential temperature (θ_e, solid) and quadrant-mean saturation equivalent potential temperature (θ_{es}, dashed) in (a) RI, (b) SI, and (c) NI cases.

both. Figure 5 shows the deviation from the azimuthal mean of specific humidity and potential temperature (θ) in each shear-relative quadrant. Consistent with the azimuthal variations in θ_e, the mean specific humidity and mean θ in the lowest kilometer also reached a maximum in the USR quadrant and a minimum in the left of shear quadrants in the RI cases (Figs. 5a,b). The 0–1-km mean specific humidity was about 0.7 g kg^{-1} larger in the USR quadrant than the USL quadrant, and the 0–1-km mean θ was about 0.5 K warmer in the USR quadrant than the left of shear quadrants. Both of these differences were statistically significant at the 95% level. At 2–3 km altitude, the mean θ was 1.5 K warmer in the USR quadrant than the DSL quadrant, consistent with the significant difference in mean θ_{es}.

As in the RI cases, the SI cases (Fig. 4b) also had the maximum 0–1-km mean θ_e in the right of shear quadrants and the minimum 0–1-km θ_e in the left of shear quadrants. The difference in 0–1-km mean θ_e between the right and left of shear quadrants was about 3–4 K and was statistically significant at the 95% level. The maximum (minimum) 0–1-km θ_{es} was also found in the right (left) of shear quadrants, with a difference in 0–1-km mean θ_{es} of about 4–6 K that was significant at the 95% level. The azimuthal variations in θ_e and θ_{es} in the lowest kilometer were slightly larger in the SI cases than the RI cases. Above 1-km altitude, θ_e continued to be maximized (minimized) in the right (left) of shear quadrants, but the quadrant differences were smaller and statistically insignificant. As in the RI cases, the mean θ_{es} in the USR quadrant was about 4 K larger than the DSL quadrant at 1.5–3 km altitudes in the SI cases. Consistent with the observed azimuthal variations in θ_e, the right of shear quadrants were moister and warmer than the left of shear quadrants, and these differences were statistically significant at the 95% level (Figs. 5c,d). The 0–1-km mean specific humidity was about 0.7 g kg^{-1} larger in the DSR quadrant than the DSL quadrant, and the 0–1-km mean θ was about 0.8 K larger in the USR quadrant than the DSL quadrant.

The observed azimuthal distribution of 0–1-km θ_e and θ_{es} in the RI and SI cases, with the maximum occurring right of shear and the minimum occurring left of shear, is consistent with downdraft modification of the boundary layer and downstream recovery through surface enthalpy fluxes, as also shown by prior modeling and observational studies (e.g., Riemer et al. 2010; Zhang et al. 2013; Tao and Zhang 2014; Finocchio et al. 2016; Nguyen et al. 2017). In the Zhang et al. (2013) composite study, which looked at hurricanes of predominantly greater than category 2 intensity (>49 m s^{-1}), the maximum θ_e was found in the DSR quadrant, as opposed to the USR quadrant in the RI and SI cases in this study. Also, the difference between the maximum θ_e DSR and the minimum θ_e DSL in the Zhang et al. (2013) study was smaller, about 1 K, compared to the 2–4 K difference found in the RI and SI cases in this study. This is likely because the Zhang et al. (2013) study focused on the eyewall region and included storms with a much-stronger mean intensity. The stronger surface enthalpy fluxes within the eyewall and within these more intense storms would allow the θ_e to recover much more quickly as the air is advected azimuthally around the storm.

In contrast to the RI and SI cases, the NI cases (Fig. 4c) exhibited reduced 0–1-km θ_e values and less azimuthal variation in 0–1-km θ_e and θ_{es}. Although the θ_e maximum (minimum) was in the USR (USL) quadrant in the lowest 500 m, the θ_e difference between these quadrants was only about 1 K and not statistically significant. Above 1.5-km altitude, the mean θ_e in each quadrant

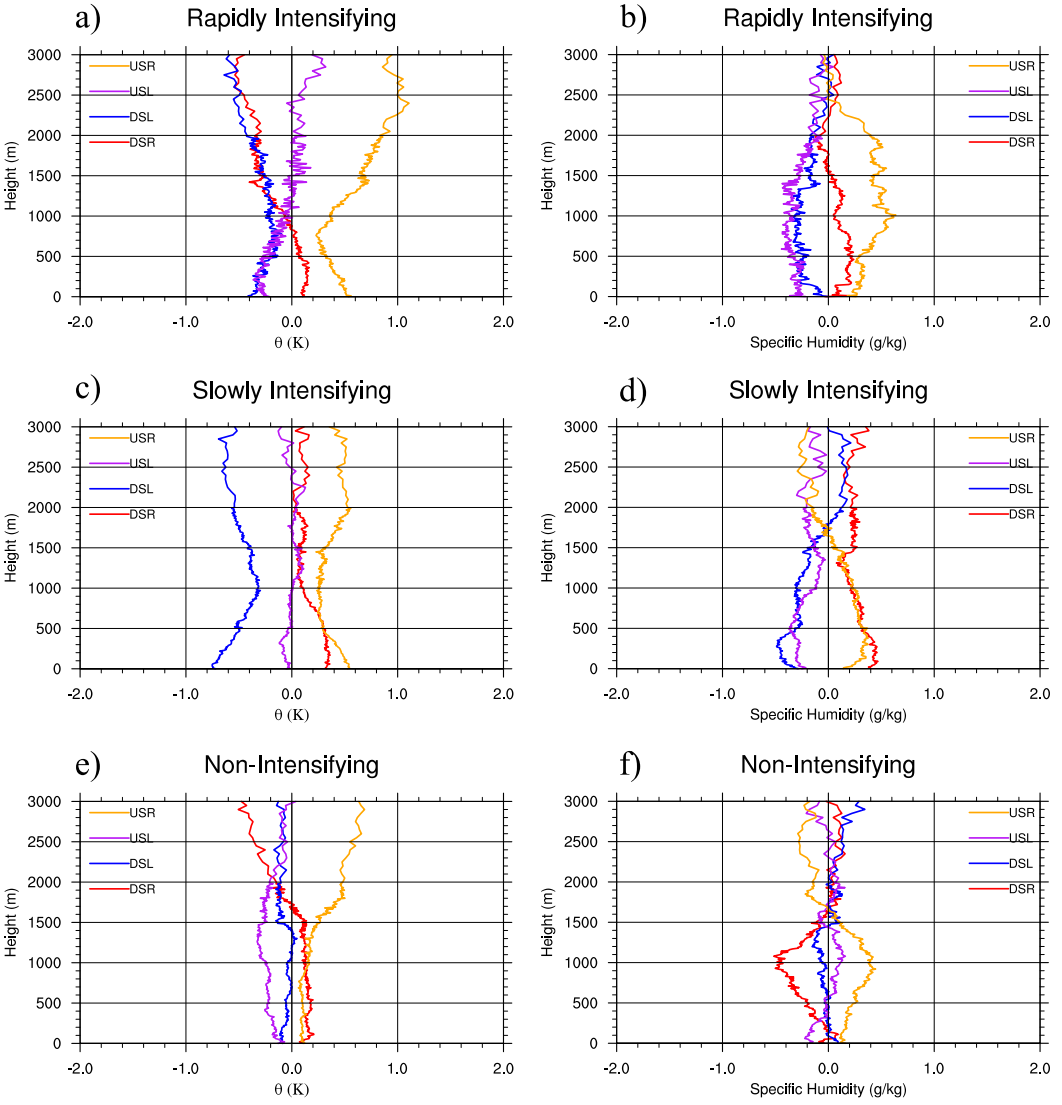

FIG. 5. Deviation from the azimuthal mean of potential temperature and specific humidity in (a),(b) RI, (c),(d) SI, and (e),(f) NI cases.

was essentially indistinguishable. Consistent with the muted azimuthal variation in θ_e, the azimuthal variation in mixing ratio and θ was also reduced (Figs. 5e,f). As in the RI and SI cases, the NI cases also exhibited higher 1.5–3-km θ_{es} in the USR quadrant than in the other quadrants. The lack of azimuthal variation in near-surface θ_e and θ_{es} may be due to reduced surface latent and sensible heat fluxes from the ocean in the NI cases, preventing the θ_e and θ_{es} from recovering as the air was advected azimuthally from left of shear to right of shear. Evidence for this will be presented in an upcoming section.

One might expect the lower-tropospheric θ_e and θ_{es} in all quadrants to progressively increase going toward further intensification (i.e., from NI to SI to RI), but this progression was not clearly observed in Fig. 4. However, notable differences between the intensity change regimes emerged when assessing the lower-tropospheric conditional instability, as will be shown in the following section.

4. Lower-tropospheric conditional stability

The conditional stability of the lower troposphere within a TC can be assessed by comparing the θ_e of a pseudoadiabatically lifted parcel (i.e., θ_e held constant as the parcel rises) with the θ_{es} of its immediate environment at a given altitude (Holton 2004; Nguyen et al. 2017). We define the lower-tropospheric instability index (LTI) as follows:

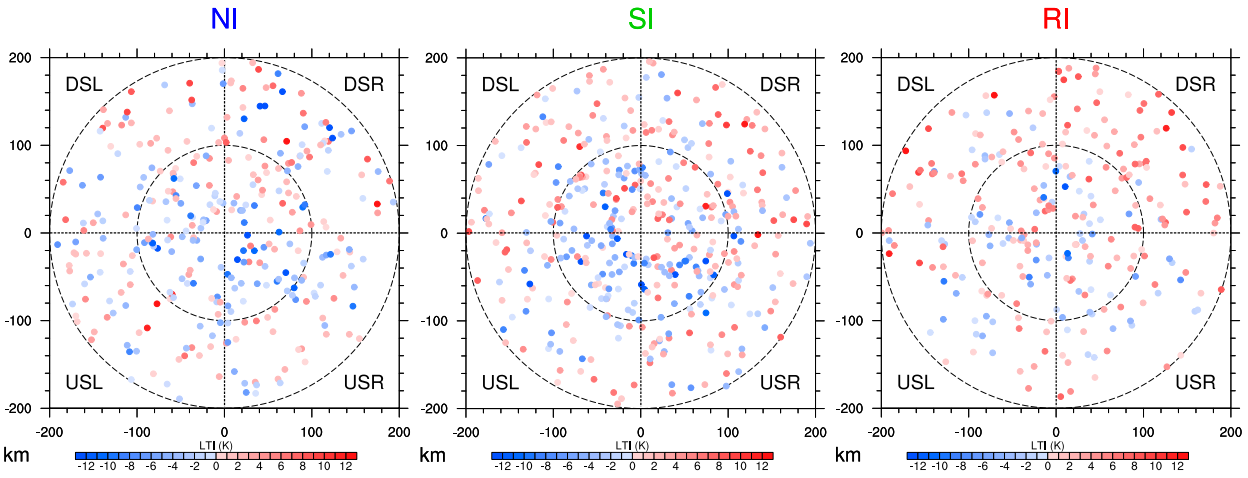

FIG. 6. Dropsondes color-coded by their lower-tropospheric instability index (LTI) in (left) NI, (middle) SI, and (right) RI storms. Positive values indicate lower-tropospheric conditional instability, while negative values indicate lower-tropospheric conditional stability. Shear vector is directed toward the top of each panel. Range rings are every 100 km. Dropsondes within 25 km of the center are omitted.

$$\mathrm{LTI} = \theta_{e,0\text{–}500\mathrm{m}} - \theta_{\mathrm{es},2\mathrm{km}}, \tag{1}$$

where $\theta_{e,0\text{–}500\mathrm{m}}$ represents the θ_e averaged over the lowest 500 m of the atmosphere, and $\theta_{\mathrm{es},2\mathrm{km}}$ represents the θ_{es} at 2-km altitude. Assuming that the lifted parcel is saturated at 2-km altitude, when the lifted parcel's θ_e exceeds the θ_{es} at 2-km altitude (LTI $>$ 0), the lifted parcel is warmer relative to its immediate environment, indicating positive buoyancy and conditional instability. On the other hand, when the lifted parcel's θ_e is less than the θ_{es} at 2-km altitude (LTI $<$ 0), the lifted parcel is cooler relative to its immediate environment, indicating negative buoyancy and conditional stability. The LTI is similar to the "lifted index" (LI) measure often used in midlatitude convection forecasting, although the LI is typically assessed at the 500 mb pressure level. Figure 6 shows individual dropsondes color coded by their LTI in NI, SI, and RI storms. There was considerable variability between dropsondes in each of the intensity change bins, which is to be expected given the small-scale updrafts, downdrafts, and precipitation features within tropical cyclones that can have thermodynamic impacts. However, upon closer inspection, there appears to be a larger proportion of sondes with positive LTI values (indicative of conditional instability) in the DSR quadrant compared to the USL quadrant, and there also appears to be more sondes with positive LTI values in the RI cases compared to the NI cases.

To quantify the differences in LTI between intensity change groups, Fig. 7 shows the distribution of LTI values displayed in Fig. 6. In all the intensity change bins, the DSR quadrant was the most unstable quadrant, while the USR and USL quadrants were the least unstable quadrants. Note that the USR quadrant was quite stable relative to the other quadrants despite the boundary layer θ_e being maximized there. The reduced lower-tropospheric conditional instability in the USR quadrant was due to warmer lower-tropospheric temperatures above the boundary layer, evidenced by the θ_{es} bowing out toward the right at around 1.5–2.5 km altitude (Fig. 4) as well as the higher θ values (Fig. 5). These warmer temperatures could be due to subsidence associated with the balanced response to the vortex tilt (Jones 1995), as the USR quadrant is typically in the uptilt direction, or subsidence due to stratiform precipitation evaporating in unsaturated air (Dolling and Barnes 2012; Kerns and Chen 2015; Zawislak et al. 2016). The cooler temperatures above 1-km altitude in the DSL quadrant, particularly in the RI and SI cases,

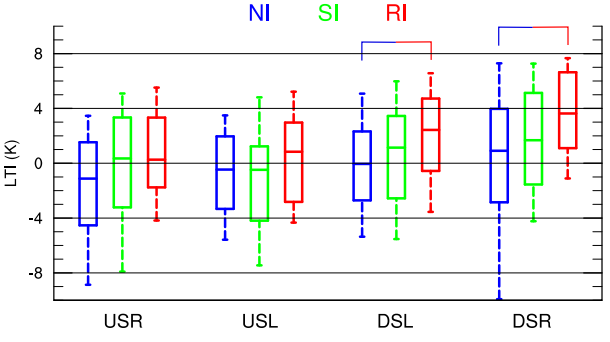

FIG. 7. Distribution of LTI values (K) in NI (blue), SI (green), and RI (red) cases in each shear-relative quadrant. Boxes encompass the 25th, 50th, and 75th percentiles, while whiskers extend to the 10th and 90th percentile values. Brackets denote the differences in the means of the distributions that were significant at the 95% confidence level as determined by a bootstrap test.

contributed to the conditional instability in that quadrant. These cooler DSL temperatures above 1-km altitude may be the result of enhanced upward motion and adiabatic cooling on the downtilt side of the tilted vortex (Jones 1995).

Interestingly, in addition to the differences between quadrants, there were also notable differences in the LTI values between intensity change bins. In the DSR and DSL quadrants, the distribution of LTI progressively shifted toward more positive values (more conditionally unstable) with increasing intensification. For example, the 50th percentile of the RI LTI distribution was roughly equal to the 75th percentile of the NI LTI distribution, while the 25th percentile of the RI LTI distribution was roughly equal to the 50th percentile of the NI LTI distribution. Also, in the DSR quadrant, negative LTI values occurred almost three times more frequently in the NI cases than the RI cases. The difference in the quadrant-mean LTI between the RI and NI cases were statistically significant at the 95% confidence level in the DSR and DSL quadrants, as determined through a bootstrap method. In the upshear quadrants, the LTI differences between the intensity change bins were smaller, as there was more overlap between the RI, SI, and NI distributions. The differences in the quadrant-mean LTI between the RI, SI, and NI cases never reached statistical significance in the upshear quadrants. It should be noted that differences in deep-tropospheric convective available potential energy (CAPE) between shear-relative quadrants and intensity change bins were also evaluated and yielded qualitatively similar results, although with a much smaller sample size due to the lack of high-altitude dropsonde data described earlier.

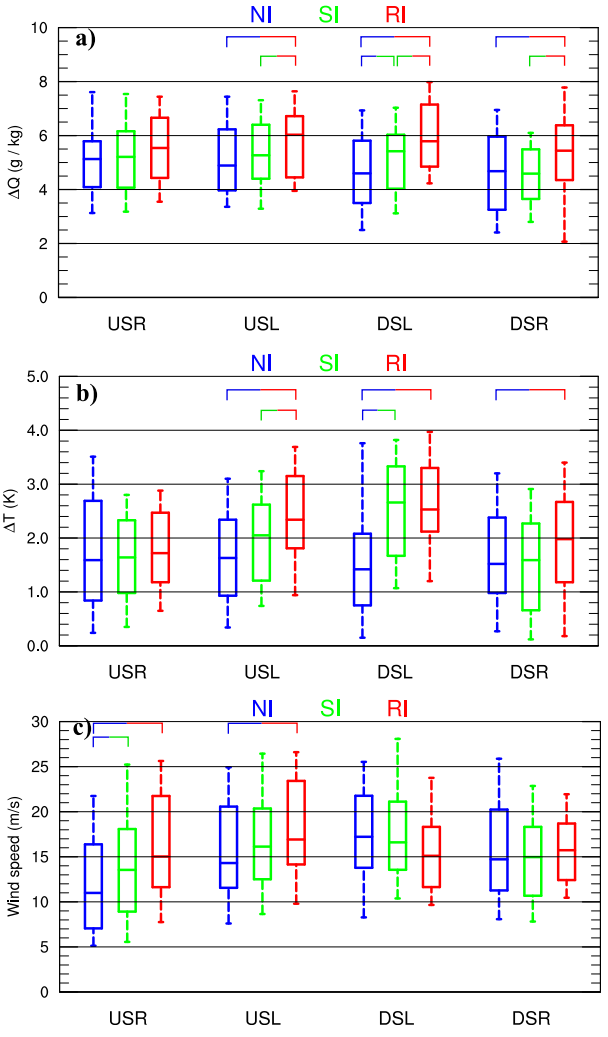

FIG. 8. Distribution of (a) $\Delta q = q_0 - q_{10}$, and (b) $\Delta T = \mathrm{SST} - T_{10}$, and (c) 10-m wind speed in NI (blue), SI (green), and RI (red) cases in each shear-relative quadrant. Brackets denote the differences in the means of the distributions that were significant at the 95% confidence level as determined by a bootstrap test.

5. Surface enthalpy fluxes

The larger DSR lower-tropospheric conditional instability in the RI cases compared to the SI and NI cases was due to the elevated boundary layer θ_e relative to the 2-km θ_{es}. An important contributor to the boundary layer θ_e in tropical cyclones is the surface enthalpy flux from the ocean. Surface latent and sensible heat fluxes were calculated using the bulk method, as follows:

$$F_q = \rho L_v C_e U_{10}(q_0 - q_{10}), \tag{2}$$

$$F_H = \rho c_p C_h U_{10}(\mathrm{SST} - T_{10}), \tag{3}$$

where ρ is the air density ($1.2\,\mathrm{kg\,m^{-3}}$); L_v is the latent heat of vaporization ($2.5 \times 10^6\,\mathrm{J\,kg^{-1}}$); c_p is the specific heat capacity of air at constant pressure ($1004.64\,\mathrm{J\,kg^{-1}\,K^{-1}}$); C_e and C_h are the exchange coefficients for latent and sensible heat transfer, respectively (estimated as 1.2×10^{-3}, Zhang et al. 2008; Bell et al. 2012); U_{10} is wind speed at 10-m height; q_{10} and T_{10} are the specific humidity and temperature at 10-m height, respectively; and q_0 is the saturation specific humidity at the sea surface calculated using the SST. Dropsondes that did not report a 10-m wind speed, specific humidity, or temperature were excluded from the enthalpy flux calculation.

Figure 8 shows the distribution of the air–sea contrast in specific humidity ($\Delta q = q_0 - q_{10}$), the air–sea contrast in temperature ($\Delta T = \mathrm{SST} - T_{10}$), and the 10-m wind speed for the RI, SI, and NI cases. Although there was variability between quadrants and intensity change bins, the air–sea contrast in specific humidity generally ranged from 3 to $7\,\mathrm{g\,kg^{-1}}$, while the air–sea contrast in

temperature ranged from 1 to 3 K. While the SSTs used in the current study were primarily satellite-derived and of daily time resolution, these Δq and ΔT values compared favorably with prior studies using more sophisticated SST measurements. For example, in their composite study using buoy observations in hurricanes, Cione et al. (2013) found mean Δq values from 4 to 5 g kg^{-1} and mean ΔT values from 1.5 to 2 K. In a case study of Hurricane Edouard (2014) using SSTs observed by both airborne expendable bathythermographs (AXBT) and infrared dropsondes (IRsonde), Zhang et al. (2017) found that when Edouard was an intensifying category 2 hurricane, the Δq and ΔT values were around 3–6 g kg^{-1} and 2–4 K, respectively, within the inner core. Using SST analyses derived from fixed and drifting buoys, Jaimes et al. (2015) found Δq and ΔT values of near 5–7 g kg^{-1} and 2–4 K, respectively, within TC Earl (2010) during the intensifying tropical storm to category 2 hurricane stage. These studies give us confidence that the SST dataset used to calculate surface enthalpy fluxes in the current study were reasonable.

Statistically significant (at the 95% level) differences in Δq between the intensity change categories were present in the DSR, DSL, and USL quadrants (Fig. 8a). These differences were most pronounced in the DSL and USL quadrants, where the difference in Δq between the RI and NI medians was about 1 g kg^{-1} compared to 0.50–0.75 g kg^{-1} in the right of shear quadrants. Differences in ΔT between intensity change bins were also most pronounced in the left of shear quadrants (Fig. 8b), where the difference in ΔT between the RI/SI and NI medians ranged between 0.75 and 1.25 K (Fig. 8b). In contrast to Δq and ΔT, 10-m wind speed differences between intensity change bins were most pronounced in the upshear quadrants (Fig. 8c), with the median 10-m wind speed in RI cases exceeding the median in NI cases by 3–4 m s^{-1} (statistically significant at the 95% confidence level). In the downshear quadrants, the differences in 10-m wind speed between intensity change bins were smaller, and the difference in the means of the intensity change bins failed to reach statistical significance.

These differences in Δq, ΔT, and 10-m wind speed between intensity change regimes resulted in significant differences in surface enthalpy flux. Figure 9 shows the distribution of surface latent and sensible heat flux in the RI, SI, and NI cases. As to be expected in a TC environment, the total surface enthalpy flux was dominated by the contribution from the latent heat flux. Within each intensity change bin, the surface latent and sensible heat flux was generally larger in the left of shear quadrants than the right of shear quadrants. In all shear-relative quadrants, the RI cases had larger latent and

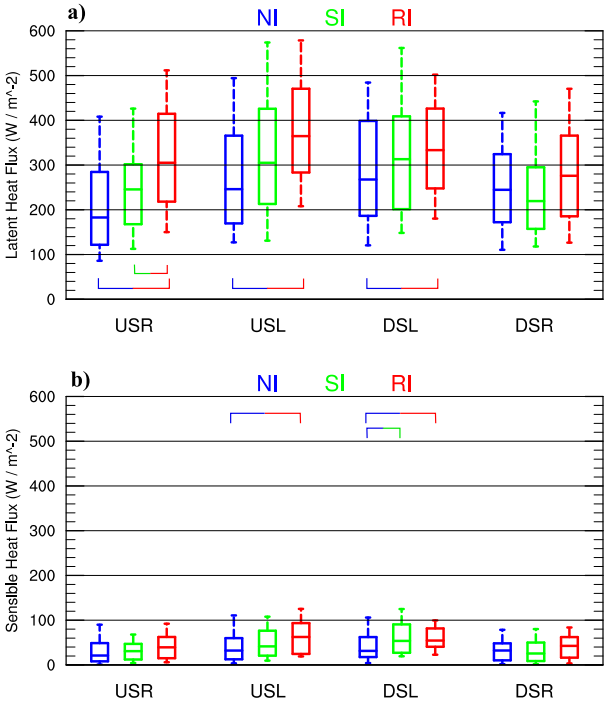

FIG. 9. Distribution of surface (a) latent heat flux and (b) sensible heat flux in NI (blue), SI (green), and RI (red) cases in each shear-relative quadrant. Brackets denote the differences in the means of the distributions that were significant at the 95% confidence level as determined by a bootstrap test.

sensible heat fluxes than the SI and NI cases. The differences in the fluxes between intensity change bins were most pronounced in the upshear quadrants. In the USL quadrant, the median latent heat flux was 246 W m^{-2} in the NI cases, 305 W m^{-2} in the SI cases, and 365 W m^{-2} in the RI cases. The 25th and 75th percentiles of latent heat flux in the RI cases also exceeded that of the NI cases by about 110 W m^{-2}. The median USL sensible heat flux in the RI cases (63 W m^{-2}) doubled the median USL sensible heat flux in the NI cases (32 W m^{-2}). In the USR quadrant, the median latent and sensible heat flux in the RI cases was about 122 W m^{-2} and 18 W m^{-2} larger than the NI cases, respectively. In contrast to the upshear quadrants, the differences in latent and sensible heat flux between intensity change bins were muted in the DSR quadrant, with the distributions largely overlapping each other.

As shown in Eqs. (2) and (3), the surface latent and sensible heat fluxes are a function of both near-surface wind speed as well as the air–sea contrast in specific humidity and temperature. Thus, it is informative to diagnose whether differences in surface fluxes between intensity change bins were attributed to differences in near-surface wind speed, differences in the air–sea specific humidity contrast, or differences in the air–sea

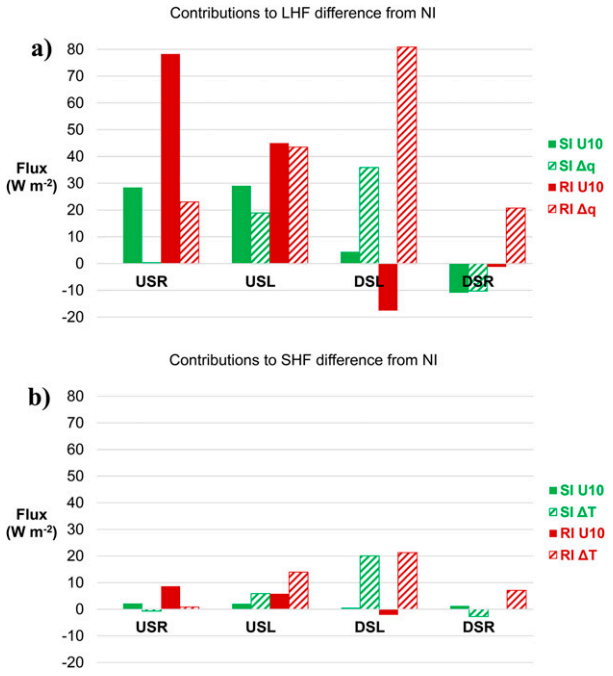

FIG. 10. (a) Latent and (b) sensible heat flux differences from the NI mean attributed to differences in mean 10-m wind speed (solid), Δq [hatched in (a)], and ΔT [hatched in (b)] in each shear-relative quadrant.

temperature contrast. Figure 10 shows the individual contributions of the difference in near-surface winds, Δq, and ΔT to the observed difference in surface enthalpy flux between the RI/SI cases and the NI cases. In the downshear quadrants (particularly DSL), the larger latent and sensible heat fluxes in the RI and SI cases were almost entirely attributed to a larger Δq and ΔT, respectively, with almost no contribution from differences in the 10-m wind speed. The larger Δq and ΔT in the DSL quadrant may be due to SSTs that were on average 0.5°–0.7°C warmer in the RI and SI cases (Fig. 2b) or perhaps enhanced cooling and drying due to downdrafts in the DSL quadrant. In the USL quadrant, the faster 10-m winds and the larger Δq made a nearly equal contribution to the larger latent heat fluxes, while the larger ΔT was the dominant contributor to the larger sensible heat fluxes in the RI/SI cases, contributing about 70% of the difference. In the USR quadrant, the larger latent and sensible heat fluxes in the RI and SI cases were mostly due to faster 10-m winds, with generally little contribution from the differences in Δq and ΔT. It should be noted, however, that these results differed somewhat when compositing with respect to moderate 850–500 hPa vertical wind shear. Although the surface latent and sensible heat flux differences between intensity change groups were reproduced using 850–500 hPa shear (not shown), the larger Δq and ΔT were instead the dominant contributors to these flux differences in all quadrants, while the contribution from increased 10-m wind speeds was nearly negligible (not shown). Thus, there remains some uncertainty regarding the relative contributions of the 10-m winds and the air–sea contrast in q and T to the increase in upshear surface enthalpy fluxes with increasing intensification.

6. Summary

Surface enthalpy fluxes play an important role in restoring moisture and heat to the boundary layer within sheared TCs. A number of prior modeling (Riemer et al. 2010, 2013; Tao and Zhang 2014; Finocchio et al. 2016; Onderlinde and Nolan 2016) and observational studies (e.g., Molinari et al. 2013; Zhang et al. 2013; Nguyen et al. 2017) have shown that in storms experiencing vertical wind shear, the boundary layer in the left of shear quadrants is cooled and dried due to convective downdrafts. As this modified boundary layer air travels cyclonically around the center of the storm, surface latent and sensible heat fluxes from the ocean act to increase the moisture and heat content of the boundary layer air until θ_e and θ_{es} reach a maximum in the downshear-right quadrant, where deep convection typically initiates.

Using dropsonde data collected by various aircraft from 1996 to 2017, this study investigated the effects of downdraft modification and boundary layer recovery within storms that were experiencing moderate environmental vertical wind shear (defined here as 4.5–11.0 m s^{-1} of 850–200 hPa shear) and were relatively weak in intensity (tropical depressions, tropical storms, and category 1 hurricanes). The data were separated into three categories according to the intensity change of the storm in the 24 h following the dropsonde observation: rapidly intensifying, slowly intensifying, and nonintensifying. The main results are:

- The magnitude of surface latent and sensible heat fluxes in the upshear quadrants grew significantly larger with increasing intensification. The enhanced fluxes upshear were attributed mostly to stronger near-surface winds, with a smaller contribution from the larger air–sea contrast in specific humidity and temperature.
- The lower-tropospheric conditional instability in the downshear quadrants was significantly larger in RI storms compared to NI storms.
- The above two results are hypothesized to be related to each other in the following manner: enhanced surface fluxes on the upshear side of RI storms enabled downdraft-modified boundary layer air to moisten and warm more quickly as it traveled cyclonically around the

storm, so that by the time this air reached the downshear quadrants, its moist entropy became larger than it otherwise would have been.

An association between enhanced surface enthalpy fluxes in the upshear quadrants and the intensification of sheared storms has been shown in prior idealized modeling (Rappin and Nolan 2012; Onderlinde and Nolan 2016) and observational (Rios-Berrios and Torn 2017; Zhang et al. 2017) studies. There are differing hypotheses on how the enhanced upshear surface fluxes contribute to the intensification of sheared storms, however. Rappin and Nolan (2012) argued that the enhanced surface fluxes encouraged the downwind propagation of convection and precipitation into the upshear quadrants, resulting in a more symmetric precipitation structure. Onderlinde and Nolan (2016) showed that enhanced upshear fluxes enabled more buoyant near-surface air parcels to be ingested into the TC inner core convection. Zhang et al. (2017) argued that, without sufficient surface enthalpy fluxes, the boundary layer moist entropy would not have recovered sufficiently enough from convective downdrafts to support the development of deep convection once the boundary layer air reached the downshear quadrants. From a ventilation theory perspective, surface enthalpy fluxes play a key role in generating available potential energy that offsets the destruction of available potential energy by dry air intrusions via vertical wind shear (Tang and Emanuel 2012; Chavas 2017).

The results in this study show that the cumulative impact of the enhanced upshear surface fluxes likely contributed to the generation of significantly larger lower-tropospheric conditional instability in the downshear quadrants of RI storms. We speculate that increased lower-tropospheric instability in the downshear quadrants would be particularly beneficial for convective updrafts to initiate and grow, since updrafts typically initiate in the DSR quadrant of sheared storms (Reasor et al. 2013; Guimond et al. 2016; Rogers et al. 2016; Wadler et al. 2018). Given that deep convection rarely initiates in the upshear quadrants (Stevenson et al. 2018), the lower-tropospheric instability in the upshear quadrants may not have as much impact on the initiation and growth of convective updrafts within a sheared storm.

In summary, the enhancement of surface fluxes upshear (predominantly due to stronger surface winds) plays an important role in mitigating the effect of downdraft cooling and stabilization that has been hypothesized to hinder TC intensification in moderate shear (Nguyen et al. 2017). However, there are a number of other important influences on TC intensity change in shear that were not investigated here. These include whether or not the vortex is able to become more vertically aligned (Tao and Zhang 2015; Finocchio et al. 2016; Miyamoto and Nolan 2018), the midtropospheric drying of the upshear quadrants through vortex-scale subsidence or entrainment from the environment (Zawislak et al. 2016; Nguyen et al. 2017), and the role of precipitation modes (convective or stratiform) in modifying the upshear thermodynamic environment (Tao et al. 2017). These processes are not necessarily independent of one another, making the TC/shear interaction problem particularly complex. For example, a couple of recent studies have theorized that warmer SSTs and/or enhanced surface enthalpy fluxes helps the vortex become more vertically aligned by promoting deep convection and latent heating (Tao and Zhang 2014; Chen et al. 2018). Given the forecasting challenges that moderately sheared storms currently present, additional coordinated research is needed to connect all of these known processes together in an overarching theory, using both existing observational platforms and numerical modeling techniques.

Acknowledgments. We thank Frank Marks, Brian Tang, and two anonymous reviewers for their constructive comments on the manuscript. This work was conducted while the first author was supported by a National Research Council research associateship award.

REFERENCES

Alvey, G. R., III, J. Zawislak, and E. Zipser, 2015: Precipitation properties observed during tropical cyclone intensity change. *Mon. Wea. Rev.*, **143**, 4476–4492, https://doi.org/10.1175/MWR-D-15-0065.1.

Bell, M. M., M. T. Montgomery, and K. A. Emanuel, 2012: Air–sea enthalpy and momentum exchange at major hurricane wind speeds observed during CBLAST. *J. Atmos. Sci.*, **69**, 3197–3222, https://doi.org/10.1175/JAS-D-11-0276.1.

Bhatia, K. T., and D. S. Nolan, 2013: Relating the skill of tropical cyclone intensity forecasts to the synoptic environment. *Wea. Forecasting*, **28**, 961–980, https://doi.org/10.1175/WAF-D-12-00110.1.

Bogner, P. B., G. M. Barnes, and J. L. Franklin, 2000: Conditional instability and shear for six hurricanes over the Atlantic Ocean. *Wea. Forecasting*, **15**, 192–207, https://doi.org/10.1175/1520-0434(2000)015<0192:CIASFS>2.0.CO;2.

Chavas, D. R., 2017: A simple derivation of tropical cyclone ventilation theory and its application to capped surface entropy fluxes. *J. Atmos. Sci.*, **74**, 2989–2996, https://doi.org/10.1175/JAS-D-17-0061.1.

Chen, S. S., J. A. Knaff, and F. D. Marks, 2006: Effects of vertical wind shear and storm motion on tropical cyclone rainfall asymmetries deduced from TRMM. *Mon. Wea. Rev.*, **134**, 3190–3208, https://doi.org/10.1175/MWR3245.1.

Chen, X., Y. Wang, J. Fang, and M. Xue, 2018: A numerical study on rapid intensification of Typhoon Vicente (2012) in the South China Sea. Part II: Roles of inner-core processes. *J. Atmos. Sci.*, **75**, 235–255, https://doi.org/10.1175/JAS-D-17-0129.1.

Cione, J. J., and E. W. Uhlhorn, 2003: Sea surface temperature variability in hurricanes: Implications with respect to intensity change. *Mon. Wea. Rev.*, **131**, 1783–1796, https://doi.org/10.1175//2562.1.

——, E. A. Kalina, J. Zhang, and E. Uhlhorn, 2013: Observations of air–sea interaction and intensity change in hurricanes. *Mon. Wea. Rev.*, **141**, 2368–2382, https://doi.org/10.1175/MWR-D-12-00070.1.

Corbosiero, K. L., and J. Molinari, 2002: The effects of vertical wind shear on the distribution of convection in tropical cyclones. *Mon. Wea. Rev.*, **130**, 2110–2123, https://doi.org/10.1175/1520-0493(2002)130<2110:TEOVWS>2.0.CO;2.

Cram, T. A., J. Persing, M. T. Montgomery, and S. A. Braun, 2007: A Lagrangian trajectory view on transport and mixing processes between the eye, eyewall, and environment using a high-resolution simulation of Hurricane Bonnie (1998). *J. Atmos. Sci.*, **64**, 1835–1856, https://doi.org/10.1175/JAS3921.1.

DeHart, J. C., R. A. Houze, and R. F. Rogers, 2014: Quadrant distribution of tropical cyclone inner-core kinematics in relation to environmental shear. *J. Atmos. Sci.*, **71**, 2713–2732, https://doi.org/10.1175/JAS-D-13-0298.1.

DeMaria, M., and J. Kaplan, 1994: A Statistical Hurricane Intensity Prediction Scheme (SHIPS) for the Atlantic basin. *Wea. Forecasting*, **9**, 209–220, https://doi.org/10.1175/1520-0434(1994)009<0209:ASHIPS>2.0.CO;2.

——, M. Mainelli, L. K. Shay, J. A. Knaff, and J. Kaplan, 2005: Further improvements to the Statistical Hurricane Intensity Prediction Scheme (SHIPS). *Wea. Forecasting*, **20**, 531–543, https://doi.org/10.1175/WAF862.1.

——, C. R. Sampson, J. A. Knaff, and K. D. Musgrave, 2014: Is tropical cyclone intensity guidance improving? *Bull. Amer. Meteor. Soc.*, **95**, 387–398, https://doi.org/10.1175/BAMS-D-12-00240.1.

Dolling, K., and G. M. Barnes, 2012: Warm-core formation in Tropical Storm Humberto (2001). *Mon. Wea. Rev.*, **140**, 1177–1190, https://doi.org/10.1175/MWR-D-11-00183.1.

Finocchio, P. M., and S. J. Majumdar, 2017: A statistical perspective on wind profiles and vertical wind shear in tropical cyclone environments of the Northern Hemisphere. *Mon. Wea. Rev.*, **145**, 361–378, https://doi.org/10.1175/MWR-D-16-0221.1.

——, ——, D. S. Nolan, and M. Iskandarani, 2016: Idealized tropical cyclone responses to the height and depth of environmental vertical wind shear. *Mon. Wea. Rev.*, **144**, 2155–2175, https://doi.org/10.1175/MWR-D-15-0320.1.

Fischer, M. S., B. H. Tang, and K. L. Corbosiero, 2018: Normalized convective characteristics of tropical cyclone rapid intensification events in the North Atlantic and eastern North Pacific. *Mon. Wea. Rev.*, **146**, 1133–1155, https://doi.org/10.1175/MWR-D-17-0239.1.

Frank, W. M., and E. A. Ritchie, 2001: Effects of vertical wind shear on the intensity and structure of numerically simulated hurricanes. *Mon. Wea. Rev.*, **129**, 2249–2269, https://doi.org/10.1175/1520-0493(2001)129<2249:EOVWSO>2.0.CO;2.

Guimond, S. R., G. M. Heymsfield, P. D. Reasor, and A. C. Didlake, 2016: The rapid intensification of Hurricane Karl (2010): New remote sensing observations of convective bursts from the Global Hawk platform. *J. Atmos. Sci.*, **73**, 3617–3639, https://doi.org/10.1175/JAS-D-16-0026.1.

Hence, D. A., and R. A. Houze Jr., 2011: Vertical structure of hurricane eyewalls as seen by the TRMM Precipitation Radar. *J. Atmos. Sci.*, **68**, 1637–1652, https://doi.org/10.1175/2011JAS3578.1.

——, and ——, 2012: Vertical structure of tropical cyclone rainbands as seen by the TRMM Precipitation Radar. *J. Atmos. Sci.*, **69**, 2644–2661, https://doi.org/10.1175/JAS-D-11-0323.1.

Hock, T. F., and J. L. Franklin, 1999: The NCAR GPS dropwindsonde. *Bull. Amer. Meteor. Soc.*, **80**, 407–420, https://doi.org/10.1175/1520-0477(1999)080<0407:TNGD>2.0.CO;2.

Holton, J. R., 2004: *An Introduction to Dynamic Meteorology*. 4th ed. International Geophysical Series, Vol. 88, Academic Press, 535 pp.

Jaimes, B., L. K. Shay, and E. W. Uhlhorn, 2015: Enthalpy and momentum fluxes during Hurricane Earl relative to underlying ocean features. *Mon. Wea. Rev.*, **143**, 111–131, https://doi.org/10.1175/MWR-D-13-00277.1.

Jones, S. C., 1995: The evolution of vortices in vertical shear. I: Initially barotropic vortices. *Quart. J. Roy. Meteor. Soc.*, **121**, 821–851, https://doi.org/10.1002/qj.49712152406.

Kaplan, J., and M. DeMaria, 2003: Large-scale characteristics of rapidly intensifying tropical cyclones in the North Atlantic basin. *Wea. Forecasting*, **18**, 1093–1108, https://doi.org/10.1175/1520-0434(2003)018<1093:LCORIT>2.0.CO;2.

——, ——, and J. A. Knaff, 2010: A revised tropical cyclone rapid intensification index for the Atlantic and eastern North Pacific basins. *Wea. Forecasting*, **25**, 220–241, https://doi.org/10.1175/2009WAF2222280.1.

——, and Coauthors, 2015: Evaluating environmental impacts on tropical cyclone rapid intensification predictability utilizing statistical models. *Wea. Forecasting*, **30**, 1374–1396, https://doi.org/10.1175/WAF-D-15-0032.1.

Kerns, B. W., and S. S. Chen, 2015: Subsidence warming as an underappreciated ingredient in tropical cyclogenesis. Part I: Aircraft observations. *J. Atmos. Sci.*, **72**, 4237–4260, https://doi.org/10.1175/JAS-D-14-0366.1.

Landsea, C. W., and J. L. Franklin, 2013: Atlantic hurricane database uncertainty and presentation of a new database format. *Mon. Wea. Rev.*, **141**, 3576–3592, https://doi.org/10.1175/MWR-D-12-00254.1.

Leighton, H., S. Gopalakrishnan, J. A. Zhang, R. F. Rogers, Z. Zhang, and V. Tallapragada, 2018: Azimuthal distribution of deep convection, environmental factors, and tropical cyclone rapid intensification: A perspective from HWRF ensemble forecasts of Hurricane Edouard (2014). *J. Atmos. Sci.*, **75**, 275–295, https://doi.org/10.1175/JAS-D-17-0171.1.

Miyamoto, Y., and D. Nolan, 2018: Structural changes preceding rapid intensification in tropical cyclones as shown in a large ensemble of idealized simulations. *J. Atmos. Sci.*, **75**, 555–569, https://doi.org/10.1175/JAS-D-17-0177.1.

Molinari, J., and D. Vollaro, 2010: Rapid intensification of a sheared tropical storm. *Mon. Wea. Rev.*, **138**, 3869–3885, https://doi.org/10.1175/2010MWR3378.1.

——, ——, and K. L. Corbosiero, 2004: Tropical cyclone formation in a sheared environment: A case study. *J. Atmos. Sci.*, **61**, 2493–2509, https://doi.org/10.1175/JAS3291.1.

——, J. Frank, and D. Vollaro, 2013: Convective bursts, downdraft cooling, and boundary layer recovery in a sheared tropical storm. *Mon. Wea. Rev.*, **141**, 1048–1060, https://doi.org/10.1175/MWR-D-12-00135.1.

Nguyen, L. T., and J. Molinari, 2015: Simulation of the downshear reformation of a tropical cyclone. *J. Atmos. Sci.*, **72**, 4529–4551, https://doi.org/10.1175/JAS-D-15-0036.1.

——, ——, and D. Thomas, 2014: Evaluation of tropical cyclone center identification methods in numerical models. *Mon. Wea. Rev.*, **142**, 4326–4339, https://doi.org/10.1175/MWR-D-14-00044.1.

——, R. F. Rogers, and P. D. Reasor, 2017: Thermodynamic and kinematic influences on precipitation symmetry in sheared tropical cyclones: Bertha and Cristobal (2014). *Mon. Wea.*

Rev., **145**, 4423–4446, https://doi.org/10.1175/MWR-D-17-0073.1.

Nolan, D. S., and L. D. Grasso, 2003: Nonhydrostatic, three-dimensional perturbations to balanced, hurricane-like vortices. Part II: Symmetric response and nonlinear simulations. *J. Atmos. Sci.*, **60**, 2717–2745, https://doi.org/10.1175/1520-0469(2003)060<2717:NTPTBH>2.0.CO;2.

——, Y. Moon, and D. P. Stern, 2007: Tropical cyclone intensification from asymmetric convection: Energetics and efficiency. *J. Atmos. Sci.*, **64**, 3377–3405, https://doi.org/10.1175/JAS3988.1.

Onderlinde, M. J., and D. S. Nolan, 2016: Tropical cyclone-relative helicity and the pathways to intensification in shear. *J. Atmos. Sci.*, **73**, 869–890, https://doi.org/10.1175/JAS-D-15-0261.1.

Rappin, E. D., and D. S. Nolan, 2012: The effect of vertical shear orientation on tropical cyclogenesis. *Quart. J. Roy. Meteor. Soc.*, **138**, 1035–1054, https://doi.org/10.1002/qj.977.

Reasor, P. D., and M. T. Montgomery, 2015: Evaluation of a heuristic model for tropical cyclone resilience. *J. Atmos. Sci.*, **72**, 1765–1782, https://doi.org/10.1175/JAS-D-14-0318.1.

——, ——, and L. D. Grasso, 2004: A new look at the problem of tropical cyclones in vertical shear flow: Vortex resiliency. *J. Atmos. Sci.*, **61**, 3–22, https://doi.org/10.1175/1520-0469(2004)061<0003:ANLATP>2.0.CO;2.

——, R. F. Rogers, and S. Lorsolo, 2013: Environmental flow impacts on tropical cyclone structure diagnosed from airborne Doppler radar composites. *Mon. Wea. Rev.*, **141**, 2949–2969, https://doi.org/10.1175/MWR-D-12-00334.1.

Reynolds, R. W., T. M. Smith, C. Liu, D. B. Chelton, K. S. Casey, and M. G. Schlax, 2007: Daily high-resolution blended analyses for sea surface temperature. *J. Climate*, **20**, 5473–5496, https://doi.org/10.1175/2007JCLI1824.1.

Riemer, M., and F. Laliberté, 2015: Secondary circulation of tropical cyclones in vertical wind shear: Lagrangian diagnostic and pathways of environmental interaction. *J. Atmos. Sci.*, **72**, 3517–3536, https://doi.org/10.1175/JAS-D-14-0350.1.

——, M. T. Montgomery, and M. E. Nicholls, 2010: A new paradigm for intensity modification of tropical cyclones: thermodynamic impact of vertical wind shear on the inflow layer. *Atmos. Chem. Phys.*, **10**, 3163–3188, https://doi.org/10.5194/acp-10-3163-2010.

——, ——, and ——, 2013: Further examination of the thermodynamic modification of the inflow layer of tropical cyclones by vertical wind shear. *Atmos. Chem. Phys.*, **13**, 327–346, https://doi.org/10.5194/acp-13-327-2013.

Rios-Berrios, R., and R. D. Torn, 2017: Climatological analysis of tropical cyclone intensity changes under moderate vertical wind shear. *Mon. Wea. Rev.*, **145**, 1717–1738, https://doi.org/10.1175/MWR-D-16-0350.1.

——, C. A. Davis, and R. D. Torn, 2018: A hypothesis for the intensification of tropical cyclones under moderate vertical wind shear. *J. Atmos. Sci.*, **75**, 4149–4173, https://doi.org/10.1175/JAS-D-18-0070.1.

Rogers, R., P. Reasor, and S. Lorsolo, 2013: Airborne Doppler observations of the inner-core structural differences between intensifying and steady-state tropical cyclones. *Mon. Wea. Rev.*, **141**, 2970–2991, https://doi.org/10.1175/MWR-D-12-00357.1.

——, J. Zhang, J. Zawislak, H. Jiang, G. Alvey, E. Zipser, and S. Stevenson, 2016: Observations of the structure and evolution of Hurricane Edouard (2014) during intensity change. Part II: Kinematic structure and the distribution of deep convection. *Mon. Wea. Rev.*, **144**, 3355–3376, https://doi.org/10.1175/MWR-D-16-0017.1.

Schecter, D. A., M. T. Montgomery, and P. D. Reasor, 2002: A theory for the vertical alignment of a quasigeostrophic vortex. *J. Atmos. Sci.*, **59**, 150–168, https://doi.org/10.1175/1520-0469(2002)059<0150:ATFTVA>2.0.CO;2.

Shimada, U., K. Aonashi, and Y. Miyamoto, 2017: Tropical cyclone intensity change and axisymmetricity deduced from GSMaP. *Mon. Wea. Rev.*, **145**, 1003–1017, https://doi.org/10.1175/MWR-D-16-0244.1.

Simpson, R., and H. Riehl, 1958: Mid-tropospheric ventilation as a constraint on hurricane development and maintenance. Preprints, *Tech. Conf. on Hurricanes*, Miami Beach, FL, Amer. Meteor. Soc., D4-1–D4-10.

Stevenson, S. N., K. L. Corbosiero, M. DeMaria, and J. L. Vigh, 2018: A 10-year survey of tropical cyclone inner-core lightning bursts and their relationship to intensity change. *Wea. Forecasting*, **33**, 23–36, https://doi.org/10.1175/WAF-D-17-0096.1.

Sumwalt, R. L., III, C. A. Hart, E. F. Weener, and T. B. Dinh-Zahr, 2017: Tropical cyclone information for mariners. National Transportation Safety Board Safety Recommendation Rep. DCA16MM001, 21 pp.

Tang, B., and K. Emanuel, 2010: Midlevel ventilation's constraint on tropical cyclone intensity. *J. Atmos. Sci.*, **67**, 1817–1830, https://doi.org/10.1175/2010JAS3318.1.

——, and ——, 2012: A ventilation index for tropical cyclones. *Bull. Amer. Meteor. Soc.*, **93**, 1901–1912, https://doi.org/10.1175/BAMS-D-11-00165.1.

Tao, C., H. Jiang, and J. Zawislak, 2017: The relative importance of stratiform and convective rainfall in rapidly intensifying tropical cyclones. *Mon. Wea. Rev.*, **145**, 795–809, https://doi.org/10.1175/MWR-D-16-0316.1.

Tao, D., and F. Zhang, 2014: Effect of environmental shear, sea-surface temperature, and ambient moisture on the formation and predictability of tropical cyclones: An ensemble-mean perspective. *J. Adv. Model. Earth Syst.*, **6**, 384–404, https://doi.org/10.1002/2014MS000314.

——, and ——, 2015: Effects of vertical wind shear on the predictability of tropical cyclones: Practical versus intrinsic limit. *J. Adv. Model. Earth Syst.*, **7**, 1534–1553, https://doi.org/10.1002/2015MS000474.

UCAR/NCAR–Earth Observing Laboratory, 2017: NOAA-DHA: Long-term NOAA dropsonde hurricane archive, version 2.0. UCAR/NCAR–Earth Observing Laboratory, accessed 1 May 2017, https://doi.org/10.5065/D6XG9PJ0.

Wadler, J. B., R. F. Rogers, and P. D. Reasor, 2018: The relationship between spatial variations in the structure of convective bursts and tropical cyclone intensification as determined by airborne Doppler radar. *Mon. Wea. Rev.*, **146**, 761–780, https://doi.org/10.1175/MWR-D-17-0213.1.

Wang, J. J., and Coauthors, 2015: A long-term, high-quality, high-vertical-resolution GPS dropsonde dataset for hurricane and other studies. *Bull. Amer. Meteor. Soc.*, **96**, 961–973, https://doi.org/10.1175/BAMS-D-13-00203.1.

Wilks, D. S., 1995: *Statistical Methods in the Atmospheric Sciences: An Introduction*. International Geophysics Series, Vol. 59, Elsevier, 467 pp.

Willoughby, H. E., and M. B. Chelmow, 1982: Objective determination of hurricane tracks from aircraft observations. *Mon. Wea. Rev.*, **110**, 1298–1305, https://doi.org/10.1175/1520-0493(1982)110<1298:ODOHTF>2.0.CO;2.

Zawislak, J., H. Jiang, G. Alvey, E. Zipser, R. Rogers, J. Zhang, and S. Stevenson, 2016: Observations of the structure and evolution of Hurricane Edouard (2014) during intensity change. Part I: Relationship between the thermodynamic structure and

precipitation. *Mon. Wea. Rev.*, **144**, 3333–3354, https://doi.org/10.1175/MWR-D-16-0018.1.

——, L. Nguyen, E. Paltz, K. Young, H. Voemel, and T. Hock, 2018: Development and applications of a long-term, global tropical cyclone dropsonde dataset. *33rd Conf. on Hurricanes and Tropical Meteorology,* Ponte Vedra Beach, FL, Amer. Meteor. Soc., P3.32, https://ams.confex.com/ams/33HURRICANE/webprogram/Paper339581.html.

Zhang, F., and D. Tao, 2013: Effects of vertical wind shear on the predictability of tropical cyclones. *J. Atmos. Sci.*, **70**, 975–983, https://doi.org/10.1175/JAS-D-12-0133.1.

Zhang, J. A., P. G. Black, J. R. French, and W. M. Drennan, 2008: First direct measurements of enthalpy flux in the hurricane boundary layer: The CBLAST results. *Geophys. Res. Lett.*, **35**, L14813, https://doi.org/10.1029/2008GL034374.

——, R. F. Rogers, P. Reasor, E. Uhlhorn, and F. D. Marks Jr., 2013: Asymmetric hurricane boundary layer structure from dropsonde composites in relation to the environmental wind shear. *Mon. Wea. Rev.*, **141**, 3968–3984, https://doi.org/10.1175/MWR-D-12-00335.1.

——, J. J. Cione, E. A. Kalina, E. W. Uhlhorn, T. Hock, and J. A. Smith, 2017: Observations of infrared sea surface temperature and air–sea interaction in Hurricane Edouard (2014) using GPS dropsondes. *J. Atmos. Oceanic Technol.*, **34**, 1333–1349, https://doi.org/10.1175/JTECH-D-16-0211.1.